Pure Appl. Geophys.

https://doi.org/10.1007/s00024-025-03902-z

Pure and Applied Geophysics

Sedimentary Structure of the Western Songliao Basin in Northeast China Revealed by Frequency-Dependent P-Wave Delay

RONGTAO ZHAO,[1] MEI FENG,[1] MEIJIAN AN,[1] HESHENG HOU,[1] and XIANZHI ZOU[1]

Abstract—The Songliao Basin, a major Meso-Cenozoic sedimentary basin in Northeast Asia, is well known for its significant hydrocarbon resources. The sediments beneath the Central Depression have been extensively investigated, but the western basin, including the Western Slope and Southwestern Uplift, remains relatively under-explored. For a better understanding of the sediments in the western Songliao Basin, we conducted a frequency-dependent P-wave delay analysis using waveforms from 26 temporary broadband seismic stations of a north–south linear array across the western basin from 2021 to 2023. Our results reveal a pronounced variation in the thickness of the Quaternary and Cretaceous sedimentary cover, ranging from ∼ 1.5 km in the axial part of the Western Slope to 0.5 km at the basin margin. The thicknesses also exhibit obvious variations around the Chifeng–Kaiyuan Fault and the Jiamatu Uplift, highlighting a significant relationship between sedimentation and tectonics. The resulting S-wave velocity profiles show that the sediments between the Solonker–Xar Moron Suture and the Jiamatu Uplift can be represented by a single layer, while those in the central part of the Western Slope and Southwestern Uplift exhibit a pronounced vertical negative velocity gradient. These results imply that beneath the basin-wide Nenjiang Formation, the low-velocity Qingshankou Formation, being rich in hydrocarbon resources, is likely developed in such areas with a negative velocity gradient. Consequently, the central part of the Western Slope and Southwestern Uplift may have more favorable hydrocarbon resource potential compared to other regions of the western basin, but its potential is modest compared to the Central Depression.

Keywords: Frequency-dependent P-wave delay, sedimentary thickness and S-wave velocity, western Songliao Basin, oil and gas resource potential.

1. Introduction

The Songliao Basin is a large Meso-Cenozoic sedimentary basin in NE China (Fig. 1). Its eastern part is rich in hydrocarbon resources (Z. Feng et al., 2010), and thus has attracted intensive drilling and active-source seismic explorations (e.g., Fu et al., 2019; Hou et al., 2018). However, neither of the drilling and active-source seismic explorations are economic, making the western part of the basin with less abundance of hydrocarbon resources remain under-explored.

The Songliao Basin is located in the eastern Central Asian Orogenic Belt. The Songnen Block, which constitutes the basement of the Songliao Basin, collided with the North China Craton to the south along the Solonker-Xar Moron Suture and with the Xing'an Block to the northwest along the Heihe-Hegenshan Suture during the Late Paleozoic Era (J. Li et al., 2019; Liu et al., 2017, 2021; Pan et al., 2009; Xiao et al., 2003; Zhou & Wilde, 2013). Since ∼ 200 Ma, the Songnen Block has been primarily influenced by the subduction system of the (Paleo-) Pacific Plate to the east (e.g., J. Li et al., 2019; Shinjiro et al., 1990; P. J. Wang et al., 2016), which led to the development of numerous NE-SW trending structures and intense magmatic activities within the block (China Geological Survey, 2004) and formed the Songliao Basin. The Songliao Basin developed through regional mega-rifting (150–105 Ma), significant sagging (105–79.1 Ma) characterized by higher subsidence rates in the north than in the south, and regional uplift and structural inversion (79.1–64 Ma) with a reduction in sedimentation (e.g., Z. Feng et al., 2010; P. J. Wang et al., 2016). Throughout the Cenozoic Era, with the retreat of the Pacific Plate, the

Supplementary Information The online version contains supplementary material available at https://doi.org/10.1007/s00024-025-03902-z.

---

[1] Chinese Academy of Geological Sciences, No. 26 Baiwanzhuang Street, Beijing 100037, China. E-mail: mei_feng_cn@163.com

Birkhäuser

basin has experienced minimal tectonic activity, thereby preserving its original structural framework to the present day. The Central Depression (CD in Fig. 1) is a sub-tectonic region rich in hydrocarbon resources within the basin (Z. Feng et al., 2010).

Investigating the structure of sediments is essential not only for unraveling the tectonic history of a basin and assessing hydrocarbon resources, but also is particularly useful for an investigation of the basin's crust and lithosphere using body waves (e.g., R. Zhang et al., 2023). As a low-cost and valuable complement to drilling and active-source seismic exploration, passive seismic methods have been world-widely applied in sedimentary and crustal structure studies (e.g., An et al., 2024; L. Zhang & Tian, 2024; H. Zhang et al., 2025). Surface-wave tomography of the Songliao Basin has shown that the Central Depression has significantly thicker low-velocity sediments compared to the Southwestern Uplift and possibly contains two distinct depocenters in its northern and southern parts (M. Feng et al., 2023; G. Li et al., 2016; Tang et al., 2022; R. Wang et al., 2019). However, surface-wave tomography has limitations in vertical and lateral resolution, which makes it challenging to accurately determine sediment thickness. In contrast, body-wave receiver functions are highly sensitive to impedance contrasts and can reliably detect sediment thickness. Yet, converted phases and multiples often strongly interfere with each other, making them difficult to identify and complicating the investigations (Y. Bao & Niu, 2017; Kuang et al., 2022; Tao et al., 2014; K. Zhang et al., 2020). The microtremor horizontal-to-vertical spectral ratio (H/V) is another method for estimating sediment thickness (F. Bao et al., 2019), but its reliability heavily relies on prior knowledge of sedimentary S-wave velocity. Besides, surface-wave or receiver-function analyses are often more sensitive to deeper structures (> several km), and H/V spectral ratio measurements are sensitive to very shallow layers (hundreds of meters). Given the limitations and advantages of different methods, accurately estimating sediment thickness using passive seismic methods remains a challenge.

Forward modeling (Y. Bao & Niu, 2017) has shown that converted S-waves and reverberations at the sediment–basement interface can interfere with the direct P-wave, resulting in a frequency-dependent delay of the P-wave arrival. The magnitude of this delay is governed mainly by the shear-wave velocity and thickness of the sedimentary layer. Consequently, inverting frequency-dependent P-wave delays is a robust mean for recovering these two parameters (e.g., Deng et al., 2023; Yang & Niu, 2019).

To enhance our understanding of the structure and evolution of the western Songliao Basin, the Chinese Academy of Geological Sciences deployed 26 broadband seismic stations along a ~ 500-km-long north–south line (blue triangles in Fig. 1) approximately along 123°E, from September 2021 to November 2023. This linear array (called DB array) traverses the Western Slope and Southwestern Uplift, regions that have been relatively under-sampled. The dense broadband seismic observations of the array provide a valuable opportunity to investigate the western Songliao Basin. This paper aims to conduct a P-wave delay time analysis across multiple frequency bands for the records of the broadband seismic stations along the array (Fig. 1). The resulting sedimentary velocity and thickness models will address a data gap in this relatively under-sampled region and refine our understanding of basin evolution.

2. Data

This study uses three-component waveforms from the 26 broadband seismic stations (DB01-DB26 in Fig. 1) of the DB array. The array was operational from September 2021 to November 2023. To ensure a high signal-to-noise ratio and near-vertical P-wave incidence, we selected teleseismic events with epicentral distances of 30–95° and Mw $\geq$ 5.5 (yellow circles in Fig. 1 inset). Following standard pre-processing steps, including detrending, demeaning, and instrument-response removal, the horizontal component seismograms were rotated into radial and transverse components. The vertical and radial traces were subsequently band-pass filtered across five period bands: 1–10 s, 2–20 s, 3–30 s, 4–40 s, and 5–50 s. The five period bands were set starting from 1–5 s because the maximum frequency for teleseismic P waves was normally lower than ~ 3 Hz and

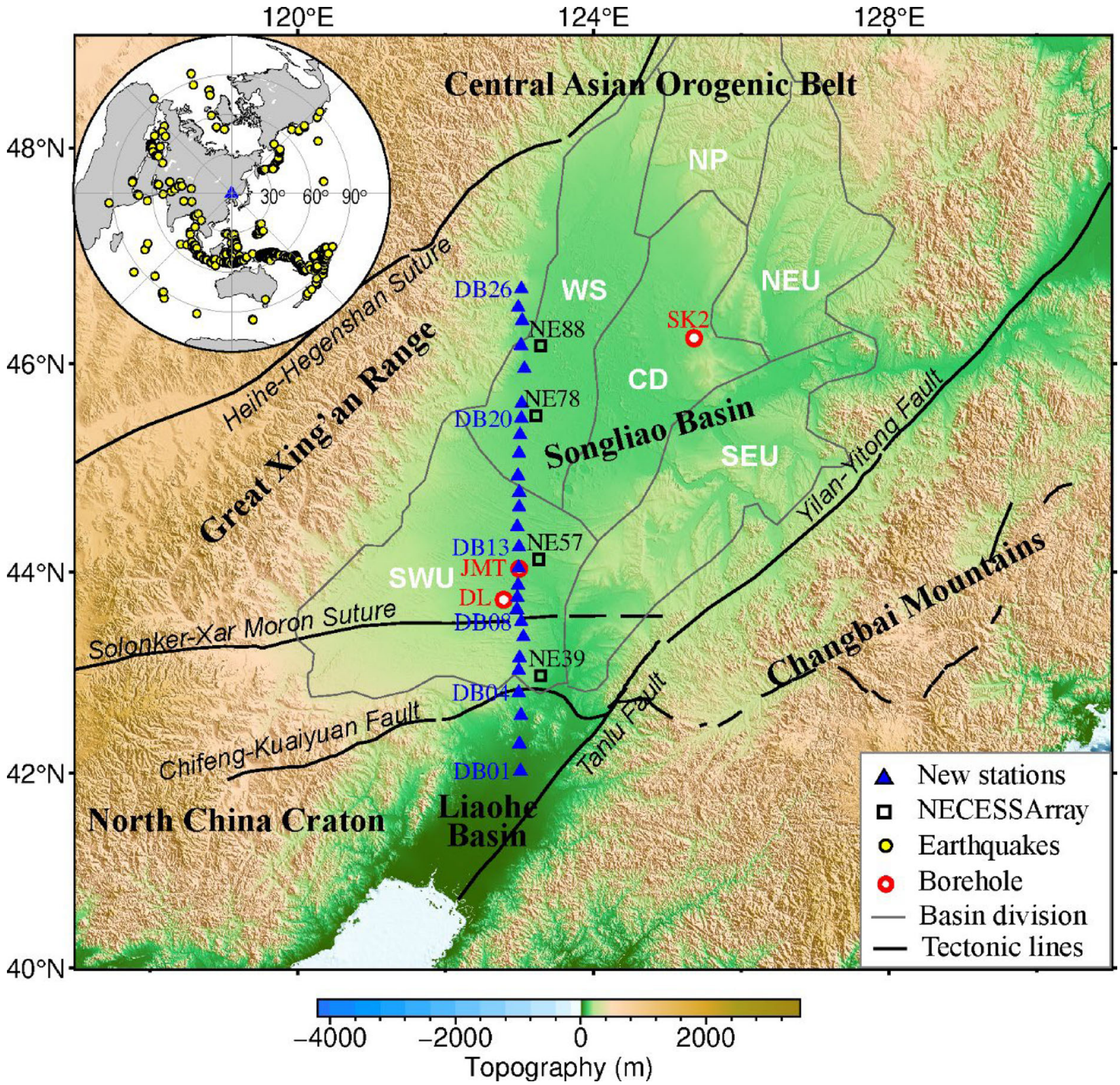

Figure 1
Tectonic settings of the Songliao Basin and the seismic stations used in this study. The upper left inset map illustrates the distribution of earthquakes (yellow circles) relative to the center of the seismic array (blue triangle). The blue triangles represent the broadband seismic stations of the DB linear array deployed by the Chinese Academy of Geological Sciences. The black squares indicate the seismic stations of NECESSArray. Sub-tectonic regions (Z. Feng et al., 2010) are labeled as follows: CD = Central Depression; NEU = Northeastern Uplift; NP = Northern Plunge; SEU = Southeastern Uplift; WS = Western Slope; SWU = Southwestern Uplift. Boreholes are also marked: SK2 = Songke-2; JMT = Jiamatu; DL = Dalin

even lower for S-waves (∼ 1 Hz) due to attenuation along long-distance propagation (Zhang & Tian, 2024) and the basement of the Songliao basin was generally not deeper than the wavelength of a 5 s signal (∼ 7–10 km) (Li et al., 2016). We extend the period bands to 10–50 s to better constrain sediment with varied thicknesses. Figure 2a shows the filtered P waveforms at stations DB04, DB08, DB13, and DB26 for the event that occurred on 11 October 2021 at 09:10:25 UT. Across all stations, the radial-

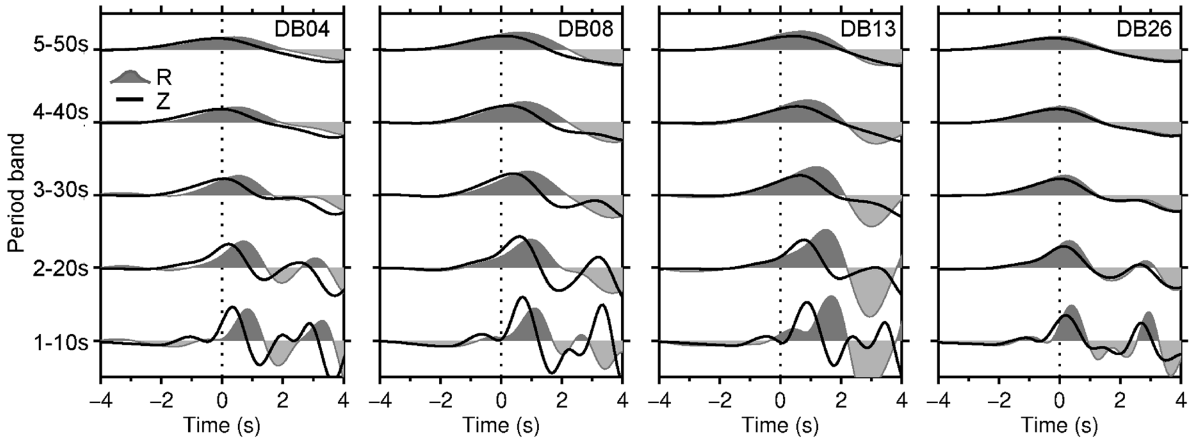

(a) Band-pass-filtered Z & R component seismograms for the 2021-10-11 09:10:25 Mw6.9 event (156.581°W, 56.295°N)

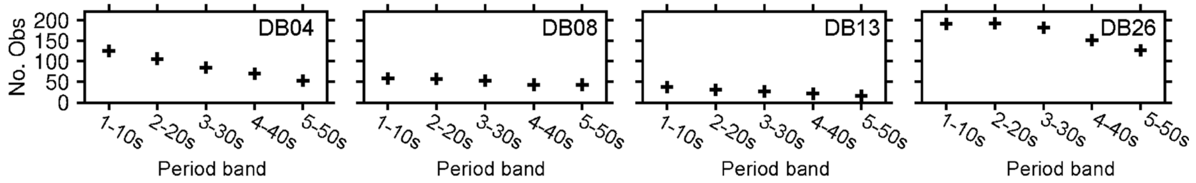

(b) Number of effective events

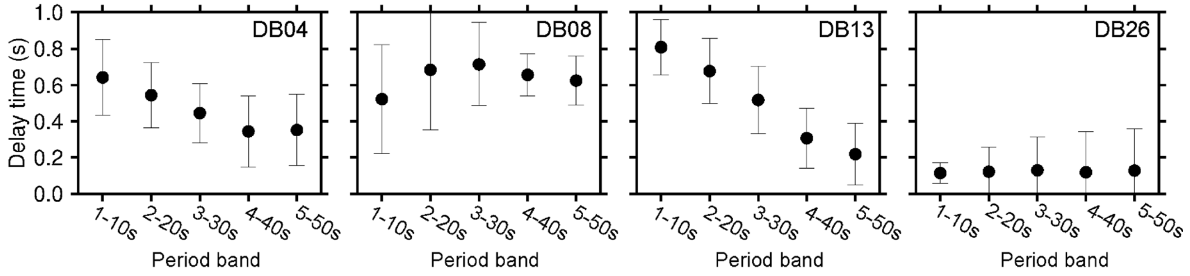

(c) Mean P-wave delay times and their standard deviations

Figure 2
Frequency-dependent P-wave delay times at four seismic stations (DB04, DB08, DB13, DB26). In panel **a**, vertical dotted lines mark the theoretical direct P arrival time

component P arrivals exhibit progressive delays relative to the vertical component as frequency increases. Although anisotropy and/or dipping interface can cause periodic delays with respect to back-azimuths (e.g., M. Feng et al., 2024, 2025), the P-wave delays in our study are only available for limited back azimuths and don't appear obvious periodic variation with respect to back-azimuths but oscillate from their total mean (Figure S2 in the Supplementary Material). So, the averaged P-wave delays from different back-azimuths used in our study can be taken as mainly arisen from differential interference between sedimentary P-to-S conversions and reverberations on the vertical and radial components (Y. Bao & Niu, 2017). It offers an approach to constrain the major (first-order) sedimentary thickness and shear-wave velocity.

We measured the P-wave delay times between the radial and vertical components of the band-pass-filtered waveforms using cross-correlation. Since sediment-induced delays beneath the Songliao Basin are typically less than 2 s (Y. Bao & Niu, 2017), we slid the radial trace within a ± 2 s window in steps equal to the sampling interval. The lag that maximized the cross-correlation coefficient was recorded as the delay time. For each station and each period band, we calculated the average delay from all usable events and determined their standard deviation. Measurements within one standard deviation of the mean were considered effective. The mean and standard deviation of these effective measurements were then adopted as the final observations. The counts of effective observations across all stations range from 11 to 229. The numbers of effective observations across the five period bands for four representative stations are shown in Fig. 2b. The mean delays and their uncertainties (standard deviations) are shown in Fig. 2c. At DB04 and DB13, delay times decrease monotonically with increasing period. DB08 exhibits an initial increase followed by a decrease, with all delays exceeding 0.5 s. In contrast, DB26 consistently exhibits small delays (< 0.2 s) across all period bands. These distinct frequency-dependent signatures suggest markedly different sedimentary structures beneath the four sites.

3. *Method*

We adopt the frequency-dependent P-wave delay-time methodology of Bao and Niu (2017), using a grid search inversion to determine the optimal sedimentary S-wave velocity and thickness. We also improved the forward modeling procedures for better reflecting more realistic stratigraphic conditions. The key aspects and enhancements of our method are detailed below.

3.1. Forward Modeling

To better understand how frequency-dependent P-wave delays are controlled by sedimentary structure, we designed four synthetic sedimentary models (black lines in Fig. 3a): a single layer of thin sediment (THIN), a single layer of thick sediment (THICK), two layers of equal thickness with a positive velocity gradient (ThickP), and two layers of equal thickness with a negative velocity gradient (ThickN). The purpose of designing these four models was to facilitate comparison with subsequent results for real data. The layer thicknesses (*Hs*) and S-wave velocities (*Vs*) are annotated in the panels of Fig. 3a. All models are supposed to be underlain by a 35-km crystalline crust with a fixed *Vs* of 3.5 km/s. Using the RAYSUM code (Frederiksen & Bostock, 2000), we generated synthetic radial (gray) and vertical (black) waveforms for each model and added random noise with an amplitude of ∼ 10% of the direct P wave. The synthetics were band-pass filtered at the same five period bands applied for the field data (1–10, 2–20, 3–30, 4–40 and 5–50 s). The resulting P waveforms are shown in Fig. 3b, where the frequency-dependent radial/vertical delays are clearly visible. The delays were measured in the same manner as for the field data (squares in Fig. 3c). The THIN model yields small, almost constant delays, indicating a weak sedimentary influence. The THICK model produces larger delays with little frequency dependence. ThickP exhibits delays that increase as frequency decreases, whereas ThickN shows the opposite trend—delays decrease with decreasing frequency. These forward-modeling results confirm that frequency-dependent P-wave delays are highly sensitive to sedimentary structure and thus provide robust constraints for inversion.

3.2. Grid Search for Sedimentary Thickness and S-Wave Velocity

We determined the optimal sedimentary thickness (*Hs*) and S-wave velocity (*Vs*) using grid search. Within predefined bounds, this method systematically evaluates every pair of (*Hs*, *Vs*) at fixed increments. For each candidate model (Hs_i, Vs_i), synthetic waveforms are generated and processed in the same manner as described in the forward-modeling section. The best-fit model is identified as the one that minimizes the misfit between the observed and predicted frequency-dependent P-wave delays. This misfit is quantified by the objective function:

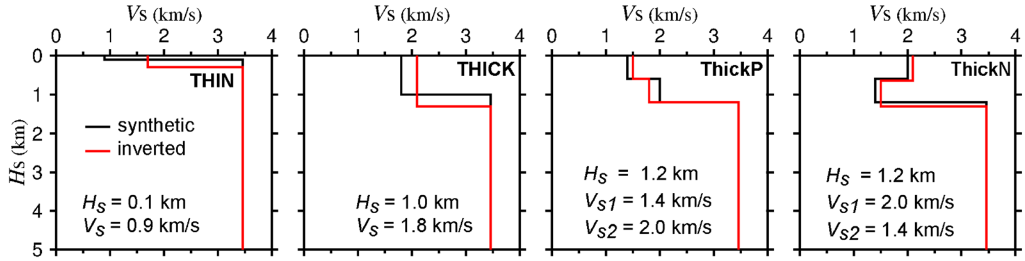

(a) Synthetic sedimentary models

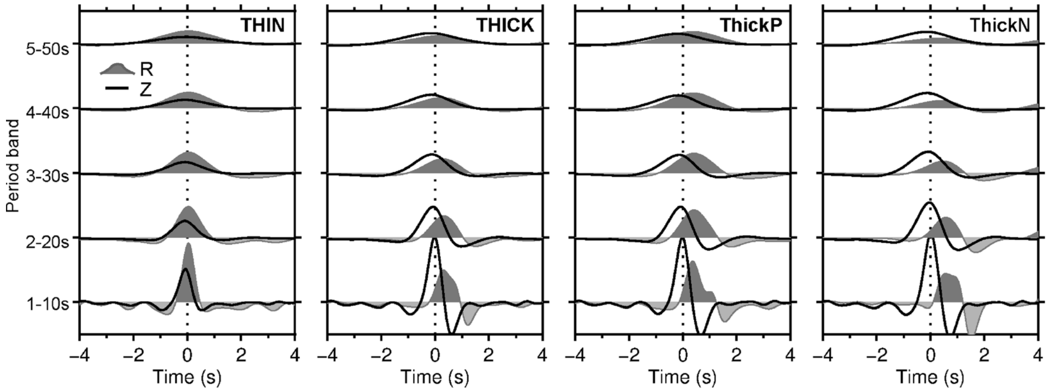

(b) Synthetic P waveforms

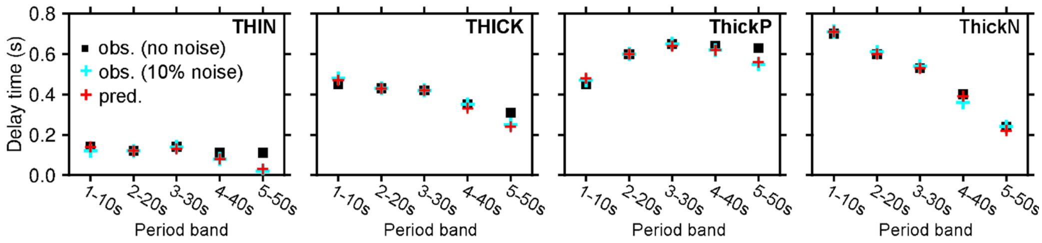

(c) P-wave delay times

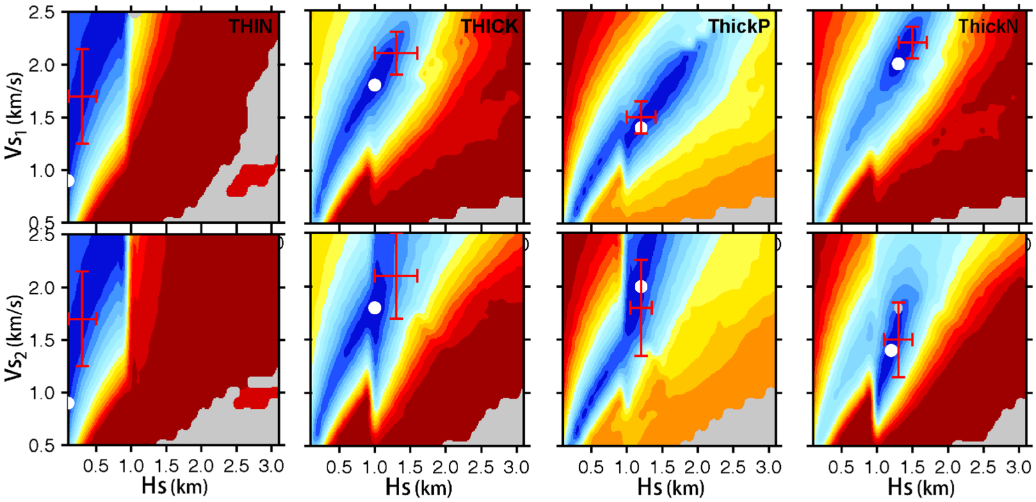

(d) Normalized misfit distributions in solution space

◀Figure 3
Four synthetic sedimentary models (**a**), and their synthetic P waveforms (**b**), frequency-dependent P-wave delay times (**c**), and normalized misfit distributions in solution space (**d**). In panel **b**, synthetic seismograms are contaminated with random noise at $\sim$ 10% of the direct P-wave amplitude. In panel **c**, black squares and cyan crosses are P-wave delays measured from noise-free and noise-contaminated data; red crosses are predicted P-wave delays from the inverted models. In panel **d**, the color scale ranges from blue (low) to red (high), indicating increasing misfit; white dots mark the true models, while red crosses denote the inverted models along with their uncertainties

$$\text{misfit} = \sqrt{\frac{1}{N}\sum_{i=1}^{N}\frac{(t_{oi}-t_{pi})^2}{\sigma_{oi}^2}} \tag{1}$$

where N denotes the number of period bands; t_{oi} and t_{pi} are the observed and predicted P-wave delay times for the i-th band; and σ_{oi} is the corresponding observational standard deviation.

We initially assumed a single sedimentary layer. Guided by prior estimates of S-wave velocity (*Vs*) and thickness (*Hs*) for the Songliao Basin (Y. Bao & Niu, 2017; G. Li et al., 2016; R. Zhang et al., 2023), we conducted a grid search for *Vs* from 0.5 to 2.5 km s^{-1} in increments of 0.1 km s^{-1} and for *Hs* from 0 to 3 km in steps of 0.1 km. For stations where the minimum misfit remained higher than half of the average observational standard deviations of all period bands (black bars in Fig. 2c), we invoked an equal-thickness two-layer model when *Hs* is $\geq$ 1 km. The inversion then sought the optimal total thickness (*Hs*) and the velocities of the upper (Vs_1) and lower (Vs_2) layers over the same ranges and steps as the single-layer search. Vs_1 can be smaller than, equal to or greater than Vs_2, simulating sediments with single layer ($Vs_1 = Vs_2$), positive vertical *Vs* gradient ($Vs_1 < Vs_2$) or negative vertical *Vs* gradient ($Vs_1 > Vs_2$). Comparatively, the method of Bao and Niu (2017) tries to search for *Hs* and *Vs* at the Earth's surface with a zero or positive vertical *Vs* gradient, preventing detection of possible sediment layers with negative *Vs* gradient. Due to the inherent trade-off between *Hs* and *Vs*, comparable delay patterns can be produced by adjusting either *Hs* or *Vs* (to be further discussed later). Our assumption of equal thickness for the two-layer model can be compensated by varying Vs_1 and Vs_2. For any quasi-vertically incident P waves, the P-wave delays generated by converted S waves at the base of single- or multiple-layer sediments can be approximated as:

$$t = \frac{Hs}{Vs} \approx \sum_{i=1}^{n}\left(\frac{Hs}{n}\frac{1}{Vs_i}\right)$$
$$\frac{1}{Vs} \approx \frac{1}{n}\sum_{i=1}^{n}\left(\frac{1}{Vs_i}\right) \tag{2}$$

where n denotes the number of layers, *Hs* and *Vs* are the sediment thickness and S-wave velocity for the single-layer model or the total sediment thickness and its equivalent average S-wave velocity for the multi-layer models.

Figure 3d shows the normalized misfit distribution in the single- (or upper-) layer solution space for the four test cases shown in Fig. 3a (blue → red indicates increasing misfit). White dots mark the true (*Hs*, *Vs*) pairs, while red crosses denote the inverted solutions. All red crosses cluster within the low-misfit belt and lie close to the white dots, demonstrating that the grid search approach reliably recovers the underlying structure. However, the elongated misfit pattern reveals a pronounced trade-off between *Hs* and *Vs*: proportional increases (or decreases) in *Hs* and *Vs* may yield nearly identical misfit. Consequently, the inverted models (red lines in Fig. 3a) deviate slightly from the true models (black lines). Nevertheless, the inverted models faithfully capture the essential features—thin versus thick sediments and two-layer sediments with positive and negative velocity gradients. The deviations follow a systematic pattern: *Hs* and *Vs* are positively correlated, meaning an overestimate of *Hs* is compensated by an overestimate of *Vs* (Fig. 3a, THIN, THICK, and THICKP); while Vs_1 and Vs_2 of a two-layer model are anticorrelated, meaning an overestimate of Vs_1 is compensated by an underestimate of Vs_2 with their mean unchanged (Fig. 3a, THICKN).

Potential limitations of the grid searching method need to be noted. For calculation efficiency, the sediments are simplified as a single- or two-layer model which is suitable for detecting the overall characteristics of sedimentary layer rather than detailed features within the strata. The synthetic tests under an assumption of fixed and unrealistic *Vs* in the half space show that our method can better restore the variation trends but not the absolute values of *Hs* and *Vs* (Fig. 3a). Thus, one is suggested to pay more attention to the relative variation pattern of *Hs* and *Vs* over the study region rather than to the absolute values of *Hs* and *Vs* of single station when discussing the results. More synthetic tests using different *Vs* in the half space can be found in Figure S1 of the Supplementary Material.

3.3. *Model Appraisal*

The quality of the models is first assessed through the fit to the data. The red crosses in Fig. 3c represent the predicted P-wave delays from the final inversion models, which fit the observed P-wave delays (squares) reasonably well. The largest residuals occur in the 5–50 s band, where the sediment thickness may be too small compared to the signal wavelength. Uncertainty is then quantified from the misfit distribution shown in Fig. 3d. Near the optimum, the misfit contours approximate a Gaussian curve. Following the approach of An et al. (2024), we fit 1-D Gaussian curves along the *Hs* and *Vs* axes and use the full width at half maximum (FWHM) as the measure of parameter uncertainties. The lengths of the red crosses in Fig. 3d correspond to these FWHM values. The magnitudes of the uncertainties are consistent with the local misfit curvature, confirming the reliability of our uncertainty estimates.

4. *Results*

Figure 4 presents inversion results for four representative stations along the DB array (Fig. 1). At DB04 and DB13, delay times decrease monotonically with increasing period (Fig. 2c), and the inverted profiles exhibit a negative velocity gradient ($V_{S1} > V_{S2}$, Fig. 4a). This pattern is similar to the forward modelling test for the ThickN model (Fig. 3a,c). At DB08, the delay pattern shows an initial rise followed by a decline (Fig. 2c), and the inverted model indicates a positive velocity gradient ($V_{S1} < V_{S2}$, Fig. 4a). This is analogous to the forward test of the ThickP model (Fig. 3a,c). DB26 displays near-constant delays of < 0.2 s across all period bands (Fig. 2c) and an exceptionally thin sedimentary cover (Fig. 4a). This is consistent with the forward test of the THIN model (Fig. 3a,c).

Figure 5a,b shows the total sedimentary thickness (*Hs*) and average S-wave velocity (*Vs*) at each station of the DB array, with numerical values provided in Table S1 of the Supplementary Material. For comparison, the figure also shows the estimates of *Hs* and *Vs* for stations of the NECESSArray derived by Bao and Niu (2017) using a similar methodology (squares). Bao and Niu (2017) originally reported *Hs*, surface *Vs*, and vertical *Vs* gradient. To facilitate comparison, we converted their surface *Vs* and gradient to a depth-average *Vs* using Eq. (2).

The DB array traverses the Southwestern Uplift and Western Slope, regions where the sedimentary thickness (*Hs*) is remarkably smaller than in the Central Depression (Fig. 5a), as expected. Beneath the DB array, *Hs* exhibits pronounced segmentation pattern: larger *Hs* in the middle and tapering towards both ends, with dramatic variations in areas crossed by major tectonic lines. A few earlier measurements (squares) adjacent to the DB array fell within the blue color range, indicating a good agreement with our results. The average S-wave velocity (*Vs*) shows clearer segmentation in our results than in previous studies (Fig. 5b). The sediments at the northern and southern ends of the array exhibit the lowest *Vs*, whereas the thickest sediments (between DB13 and DB22) are characterized by distinctly higher *Vs*, consistent with a typical uplift architecture. Comparison of Fig. 5a and Fig. 5b reveals that both *Hs* and *Vs* undergo sharp variations around major tectonics such as the Chifeng-Kaiyuan Fault (CKF).

5. *Discussion*

5.1. *Calibration of Sedimentary Layer*

The basement of the Songliao Basin, which is composed of Paleozoic metamorphic and igneous rocks, is overlain by Jurassic, Cretaceous, Paleogene, and Neogene clastic sedimentary rocks. These sedimentary rocks reach a maximum cumulative thickness of 10 km in the central part of the basin, thinning out towards the margins. The Songliao Basin

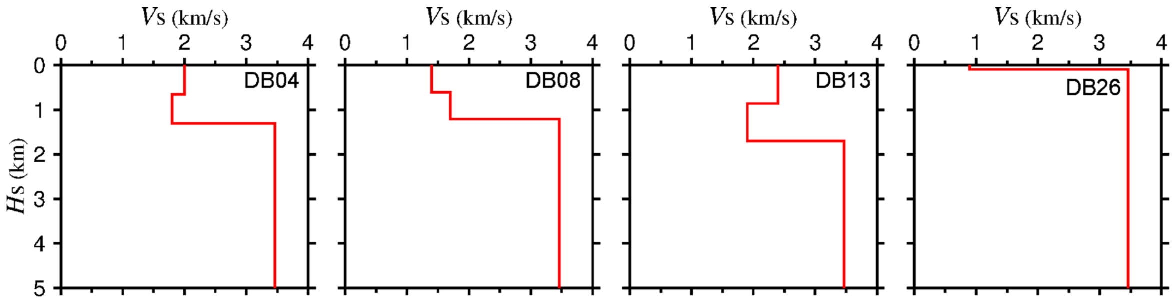

(a) Inverted sedimentary models

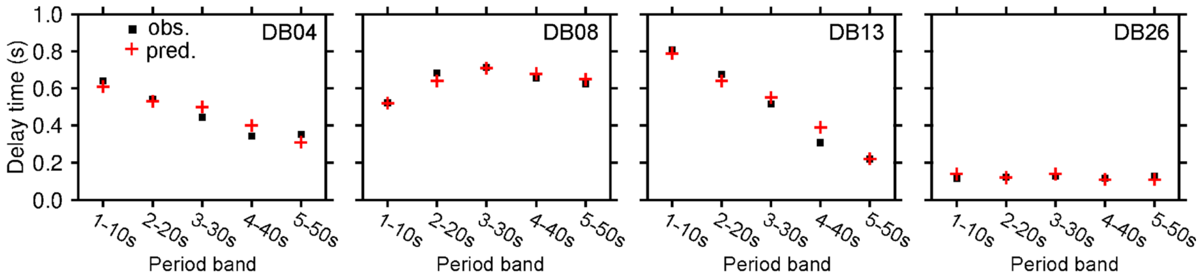

(b) P-wave delay times

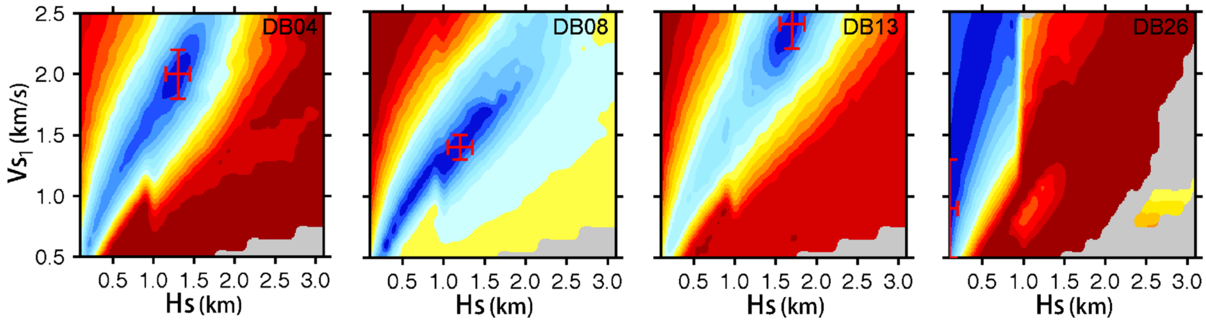

(c) Normalized misfit distributions in solution space

Figure 4
Inverted sedimentary models (**a**), fits of P-wave delay times (**b**), and normalized misfit distributions in solution space (**c**) for stations DB04, DB08, DB13, and DB26. Symbols and labels follow those in Fig. 3

evolved through three main tectonic stages: regional mega-rifting (150–105 Ma), significant sagging (105–79.1 Ma), and regional uplift and basin inversion (79.1–64 Ma) (e.g., Z. Feng et al., 2010; P. J. Wang et al., 2016) (Fig. 6a). The majority of the sedimentary rocks, particularly the three major formations of the Late Cretaceous Nenjiang Formation, Qingshankou Formation, and the Early Cretaceous Quantou Formation, were formed during the significant sagging stage. The Nenjiang Formation consists of interbedded mudstone and siltstone. The Qingshankou Formation is dominated by black shale and oil shale, characterized by a significant increase in acoustic travel time or a notable decrease in seismic wave velocity in organic-rich or porous intervals (Z. Feng et al., 2010). The Quantou Formation is primarily composed of sandstone and glutenite (Z. Feng et al., 2010; X. Wang et al.,

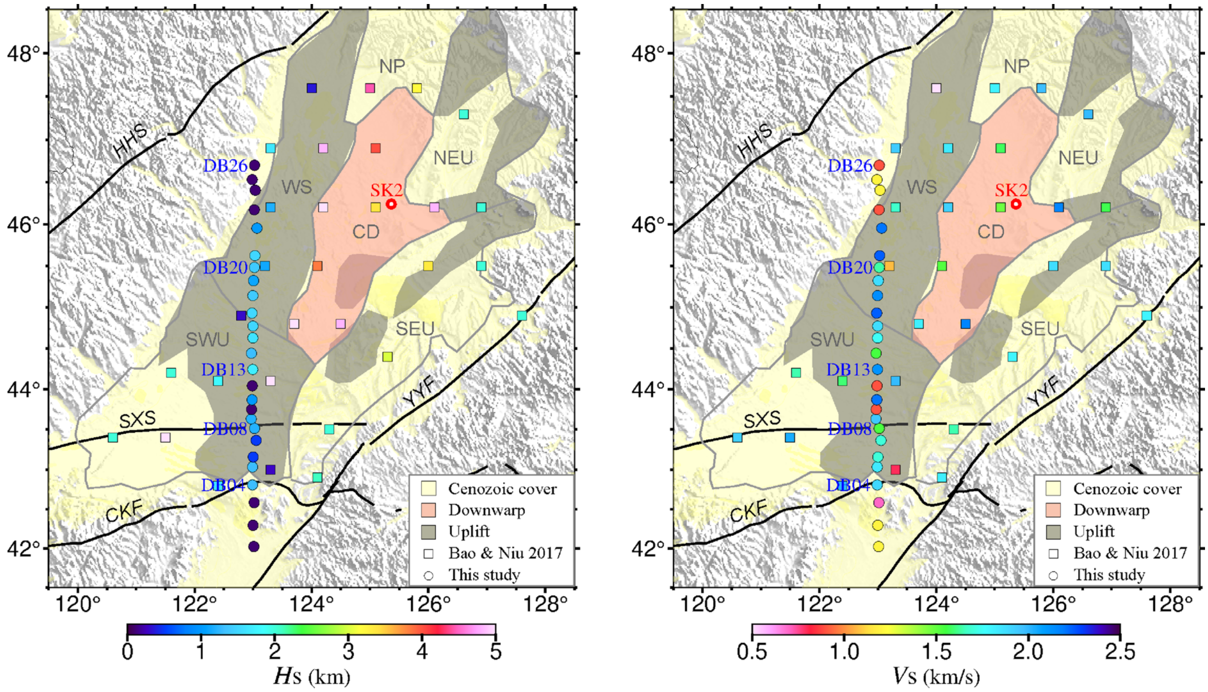

(a) Sediment thickness

(b) Average S-wave velocity

Figure 5
Sediment thickness (**a**) and average S-wave velocity (**b**) in the Songliao Basin. The squares denote results obtained by Bao and Niu (2017) using the similar methodology; their velocities have been converted to the equivalent average values via Eq. (2). Basin subdivisions are as in Fig. 1. Abbreviations are: SXS = Solonker-Xar Moron Suture; HHS = Heihe-Hegenshan Suture; YYF = Yilan-Yitong Fault; CKF = Chifeng-Kaiyuan Fault

2022a, 2022b; Xu et al., 2020) (Fig. 6a). The bases of these three major formations correspond to strong seismic reflectors T1, T2, and T3, respectively. In the Central Depression, reflectors T1 (the base of the Nenjiang Formation), T2 (the base of the Qingshankou Formation), and T3 (the base of the Quantou Formation) are at the depths of ∼ 1.4 km, ∼ 2.5, and ∼ 3.8 km, respectively. In the western part of the basin, these reflectors are shallower, with T1 at ∼ 0.9 km, T2 at ∼ 1.2 km, and T3 at ∼ 1.8 km (Z. Feng et al., 2010).

Both synthetic tests and field measurements in our DB array and in other parts of the Songliao Basin (Y. Bao & Niu, 2017) observed greater *Hs* in the basin axial region and smaller *Hs* in the margin. However, the *Hs* values adjacent to Well SK2 in the Central Depression are significantly smaller than the 6-km sedimentary thickness documented by the SK2 drill log (Fig. 5a). Although other methods consistently resolve the gross pattern of thick sediments in the center with tapering toward the margins (Kuang et al., 2022; R. Zhang et al., 2023), similar discrepancies in absolute *Hs* have been reported across the basin. These discrepancies suggest that different methods may be probing different sedimentary strata or formation. Therefore, the sediment thickness detected in our study may correspond to a specific stratum. Hence, the associated sedimentary strata should be calibrated.

Our results in the Western Slope give *Hs* ≈ 1.5–1.8 km, and a similar methodology yields *Hs* ≈ 3.0–4.0 km at Well SK2, closely matching the burial depth of the Quantou Formation revealed by seismic reflection profile (Z. Feng et al., 2010) (Fig. 6b). Moreover, the Dalin (DL) and Jiamatu (JMT) boreholes close to our DB array in the southwestern basin (locations in Fig. 1) both encountered the Quantou Formation (Guo et al., 2021). We

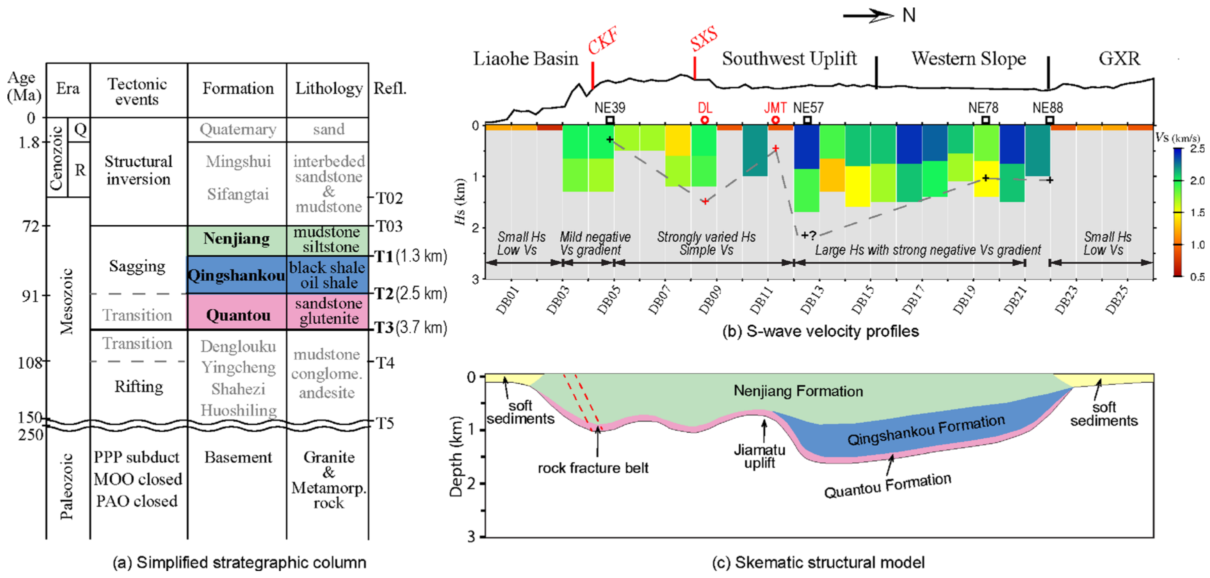

(a) Simplified strategraphic column

(b) S-wave velocity profiles

(c) Skematic structural model

Figure 6
Tectonic implications of the DB array sedimentary structures. **a** Stratigraphic column of the Central Songliao Basin simplified from P.J. Wang et al., (2016). The labeled approximate depths for T1, T2 and T3 are taken from the Central Depression of the Songliao Basin (Z. Feng et al., 2010). **b** Sedimentary structures of the DB array. **c** Schematic structural model along the DB array. In panel **b**, colored bars depict the S-wave velocity–depth profile of the sedimentary layers beneath each seismic station; the surface trace is an enlarged topography; red "+" mark sedimentary thicknesses from the DL and JMT well logs (Guo et al., 2021); black "+" denote thicknesses at NE39, NE57, NE78 and NE88 from P-wave delay time analysis (Y. Bao & Niu, 2017). Abbreviations: CKF = Chifeng Kaiyuan Fault, SXS = Solonker-Xar Moron Suture, GXR = Great Xing'an Range, PPP = (paleo-) Pacific Plate, MOO = Mongol-Okhotsk Ocean, PAO = Paleo-Asian Ocean

therefore infer that the sediments probed by our study may correspond to the base of the Quantou Formation (i.e., the T3 reflector).

5.2. *Variation of Sedimentary Thickness*

Figure 6b displays the *Vs-Hs* sedimentary profiles beneath the DB array. The overall trend of our *Hs* results (the base of the color-filled profiles) closely aligns with thicknesses derived from well logs by Guo et al. (2021) (red "+" symbols in Fig. 6b) and with those from P-wave delay time analysis by Bao and Niu (2017) (black "+" symbols). Significant sedimentary cover is observed in the Southwestern Uplift and Western Slope, with *Hs* value reaching ∼ 1.5–1.8 km in the central segment and thinning to ∼ 1.0 km at the flanks. Thickness remains modest (< 0.5 km) at both its southern end within the Liaohe Basin and its northern end in the basin-mountain transition of the Great Xing'an Range (GXR).

A striking feature in Fig. 6b is the abrupt thickness change across both the Chifeng-Kaiyuan Fault (CKF) and the Solonker-Xar Moron Suture Zone (SXS). Similar changes across tectonic lines have been previously observed in other sedimentary basins (e.g., C. Wang et al., 2022a, 2022b). The CKF and SXS were active during the late Mesozoic (Bureau of Geology & Mineral Resources of Jilin Province, 1988; G. Ma, 2018), coinciding with the sedimentation of the Qingshankou and Nenjiang formations. The observation of abrupt thickness changes across these faults highlights the significant imprint of tectonic activity on sedimentation. Dramatic thickness changes also occur between DB12 and DB13, where the Jiamatu Uplift (JMT) is located. Previous studies reported *Hs* of 5.2 km (Y. Bao & Niu, 2017) and 1.2 km (H. Ma et al., 2019) beneath NE57, a 4-km discrepancy. Our densely spaced stations DB12 and DB13 (adjacent to NE57) yield *Hs* values of 0.9 km and 2.1 km, respectively. Given the significant variations in *Hs* over such a localized uplift, our denser measurements are particularly beneficial for improving the characterization of sedimentary structures in the western Songliao Basin.

5.3. Geological Implication of Sedimentary Vs

Figure 6b reveals pronounced vertical variations in sedimentary *Vs* beneath the DB array. A mild negative *Vs* gradient, with slightly faster velocities above and slower velocities below, is observed within the Chifeng–Kaiyuan Fault zone (DB04–DB05). The section between the Solonker–Xar Moron Suture (DB09–DB12) and the Jiamatu Uplift (JMT) is characterized by a single, low *Vs* layer. Between DB13 and DB21, across the Southwestern Uplift and Western Slope, a strong negative *Vs* gradient is evident, with markedly higher *Vs* in the upper layer and lower *Vs* beneath. Sedimentary velocities are governed by lithology, porosity, fluid content, and organic richness, etc. (Gercek, 2007), all of which reflect tectonic and depositional settings. So, these segmented *Vs* patterns imply distinct tectono-sedimentary regimes along the array.

The Songliao Basin has experienced three main successive tectonic stages: rifting, subsidence, and tectonic inversion (Z. Feng et al., 2010; Wei et al., 2010; X. Wang et al., 2022a, 2022b). The Chifeng–Kaiyuan Fault, marking the basin's southern margin (Fig. 1), is a regional, deep-seated structure that was repeatedly reactivated during the Late Mesozoic when the basin was finally formed (Bureau of Geology & Mineral Resources of Jilin Province, 1988; G. Ma, 2018). As a primary basin-bounding fault, it played an important role in the multi-stage tectonic evolution of the basin. Consequently, the mild negative *Vs* gradient beneath the Chifeng–Kaiyuan Fault may be related to well-developed rock fractures in the fault zone (Fig. 6c).

Borehole logs from the southern Songliao Basin indicate that the Nenjiang Formation, which consists of interbedded mudstone and siltstone, exhibits extensive lateral continuity compared to the Qingshankou Formation (predominantly black shale and oil shale) and the Quantou Formation (characterized mainly by sandstone and glutenite) (Guo et al., 2021). When considering only lithological properties, sandstone typically exhibits a faster seismic velocity than both shale (Castagna et al., 1985; Mavko et al., 2020) and mudstone (Barton, 2006; Castagna et al., 1985; Sjögren, 1984). This suggests that the Qingshankou Formation may be more likely associated with lower seismic velocities, while the Quantou Formation may exhibit higher velocities. The Nenjiang Formation, in turn, is likely to have intermediate seismic velocities. Given the correlation between formation lithology and seismic velocities, the single sedimentary layer imaged between DB09 and DB12, located between the Solonker-Xar Moron Suture and the Jiamatu Uplift (Fig. 6b), likely corresponds to the well-developed and extensively continuous Nenjiang Formation. In contrast, the Qingshankou and Quantou Formations are relatively underdeveloped in this region.

The actual stratigraphy may be more complex than our simplified two-layer model, but a robust negative vertical *Vs* gradient persists across the Western Slope and Southwestern Uplift between DB13 and DB21. If the Western Slope and the Southwestern Uplift have undergone similar sedimentary evolution and have similar stratigraphy to the southern basin, as revealed by borehole data (Guo et al., 2021) and seismic reflection transects (H. Wang et al., 2015), the low-velocity Qingshankou Formation and the high-velocity Quantou Formation should be less-widely developed than the intermediate-velocity Nenjiang Formation in the region. Thus, our observed negative *Vs* gradient may indicate significant development of the Qingshankou Formation but limited development of the Quantou Formation (Fig. 6c). If so, the Western Slope and Southwestern Uplift between DB13 and DB21 may have more favorable hydrocarbon resource potential than the southern part between DB09 and DB12. However, since the overall sediment thickness along the DB array is much smaller than the Central Depression, the resource potential in the part with negative *Vs* gradient remains modest compared to the basin center.

6. Conclusion

The thicknesses and S-wave velocities of the sediments in the western Songliao Basin were derived from frequency-dependent P-wave delay times recorded by 26 broadband seismic stations between September 2021 and November 2023. Comparisons with borehole logs imply that the sediments targeted by our analyses are likely to extend down to the base of the Quantou Formation strata. Significant variations in sedimentary thickness were observed across the Chifeng-Kaiyuan Fault (CKF) and the Jiamatu Uplift (JMT), indicating that the sediments in the region were obviously influenced by the tectonic activities. A negative velocity gradient was detected in the central part of the Western Slope and Southwestern Uplift. This suggests that, in addition to the well-developed Nenjiang Formation, the Qingshankou Formation, which is characterized by low velocity and rich in hydrocarbon resources, may also develop in this area, implying a more favorable hydrocarbon resource potential compared to the other regions of the western basin.

Acknowledgements

This work was supported by Deep Earth Probe and Mineral Resources Exploration-National Science and Technology Major Project (No. 2024ZD1000100), Natural Science Foundation of China (42574115, 42174068) and China Geological Survey Project (DD20221829). Waveform data were provided by the Chinese Academy of Geological Sciences. All figures were generated with the Generic Mapping Tools (Wessel et al., 2013).

Author Contributions R.Z. and M.F. wrote the main manuscript text. M.A. wrote part of the data processing programs. H.H. provided project administration and financial support. X.Z. commented on the previous versions of the manuscript. All authors reviewed and approved the final manuscript.

Funding

This work was supported by Deep Earth Probe and Mineral Resources Exploration-National Science and Technology Major Project (No.2024ZD1000100), Natural Science Foundation of China (42574115, 42174068) and China Geological Survey Project (DD20221829).

Data Availability

Permission to use the data can be obtained through M.F.

Declarations

Competing Interests The authors declare no competing interests.

REFERENCES

An, M., Feng, M., Assumpção, M. S., Bianchi, M. B., França, G. S., Rocha, M. P., & Bettucci, L. S. (2024). Influence of upwelling mantle magmas on cratonic crust implied from Vp/Vs beneath South America platform. *Geophysical Journal International, 239*, 258–275. https://doi.org/10.1093/gji/ggae260

Bao, F., Li, Z., Tian, B., Wang, L., & Tu, G. (2019). Sediment thickness variations of the Tangshan Fault zone in north China from a dense seismic array and microtremor survey. *Journal of Asian Earth Sciences, 185*, Article 104045. https://doi.org/10.1016/j.jseaes.2019.104045

Bao, Y., & Niu, F. (2017). Constraining sedimentary structure using frequency-dependent P wave particle motion: A case study of the Songliao Basin in NE China. *Journal of Geophysical Research: Solid Earth, 122*, 9083–9094. https://doi.org/10.1002/2017JB014721

Barton, N. (2006). *Rock quality, seismic velocity, attenuation and anisotropy*. CRC Press. https://doi.org/10.1201/9780203964453

Bureau of Geology and Mineral Resources of Jilin Province. (1988). *Regional geology of Jilin Province* (Special Geological Report of the Ministry of Geology and Mineral Resources of the People's Republic of China, Vols. 1–10). Geological Publishing House.

Castagna, J. P., Batzle, M. L., & Eastwood, R. L. (1985). Relationships between compressional-wave and shear-wave velocities in clastic silicate rocks. *Geophysics, 50*, 571–581. https://doi.org/10.1190/1.1441933

China Geological Survey. (2004). *1:2500000 Geological map of China (in Chinese)*. China Cartographic Publishing House.

Deng, Y., Li, Z., Huang, S., Xu, Y., Hao, T., Bao, F., Zhang, S., et al. (2023). Structure of the Gonghe Sedimentary Basin in the northeastern Tibetan plateau: Evidence from teleseismic P waves recorded by a dense seismic array. *Geophysical Journal International, 235*, 1697–1711. https://doi.org/10.1093/gji/ggad327

Feng, M., An, M., Hou, H., Fan, T., & Zang, H. (2023). Channelised magma ascent and lithospheric zonation beneath the Songliao Basin, Northeast China, based on surface-wave tomography. *Tectonophysics, 862*, Article 229969. https://doi.org/10.1016/j.tecto.2023.229969

Feng, M., An, M., Qian, H., & Mechie, J. (2025). DA–H–κ: A generic method to determine 6D crustal structure by P receiver functions. *Seismological Research Letters, 96*, 2540–2549. https://doi.org/10.1785/0220240416

Feng, M., An, M., Zang, H., Assumpção, M. S., Bianchi, M. B., França, G. S., Rocha, M. P., et al. (2024). Dynamic evolution of West Gondwana inferred from crustal anisotropy of the South American platform. *Geophysical Journal International, 239*, 201–217. https://doi.org/10.1093/gji/ggae267

Feng, Z., Jia, C., Xie, X., Zhang, S., Feng, Z., & Cross, T. A. (2010). Tectonostratigraphic units and stratigraphic sequences of the nonmarine Songliao Basin, northeast China. *Basin Research, 22*, 79–95. https://doi.org/10.1111/j.1365-2117.2009.00445.x

Frederiksen, A. W., & Bostock, M. G. (2000). Modelling teleseismic waves in dipping anisotropic structures. *Geophysical Journal International, 141*, 401–412. https://doi.org/10.1046/j.1365-246x.2000.00090.x

Fu, W., Hou, H., Gao, R., Liu, C., Yang, J., & Guo, R. (2019). Fine structure of the lithosphere beneath the Well SK-2 and its adjacent: Revealed by deep seismic reflection profile. *Chinese Journal of Geophysics, 62*, 1349–1361. https://doi.org/10.6038/cjg2019M0370

Gercek, H. (2007). Poisson's ratio values for rocks. *International Journal of Rock Mechanics and Mining Sciences, 44*, 1–13. https://doi.org/10.1016/j.ijrmms.2006.04.011

Guo, Q., Xiao, J., Jia, L., Deng, F., Huang, X., & Wang, L. (2021). Study on spatial distribution characteristics of stratigraphic units in southern Songliao Basin (in Chinese with English Abstract). *Open Journal of Natural Science, 9*, 746. https://doi.org/10.12677/OJNS.2021.95081

Hou, H., Wang, C., Zhang, J., Ma, F., Fu, W., Wang, P., Huang, Y., et al. (2018). Deep continental scientific drilling engineering in Songliao Basin: Progress in earth science research (in Chinese with English Abstract). *Geology in China, 45*, 641–657. https://doi.org/10.12029/gc20180401

Kuang, C., Zhang, R., Chen, C., & Liu, J. (2022). High-resolution crustal structure in the Songliao Basin (in Chinese with English Abstract). *Acta Seismologica Sinica, 44*, 555–566. https://doi.org/10.11939/jass.20210108

Li, G., Chen, H., Niu, F., Guo, Z., Yang, Y., & Xie, J. (2016). Measurement of Rayleigh wave ellipticity and its application to the joint inversion of high-resolution S wave velocity structure beneath northeast China. *Journal of Geophysical Research: Solid Earth, 121*, 864–880. https://doi.org/10.1002/2015JB012459

Li, J., Liu, J. F., Qu, J. F., Zheng, R. G., Zhao, S., Zhang, J., Sun, L. X., et al. (2019). Major geological features and crustal tectonic framework of Northeast China. Acta Petrologica Sinica (in Chinese with English Abstract). *Acta Petrologica Sinica, 35*, 2989–3016. https://doi.org/10.18654/1000-0569/2019.10.04

Liu, Y., Li, W., Feng, Z., Wen, Q., Neubauer, F., & Liang, C. (2017). A review of the Paleozoic tectonics in the eastern part of Central Asian Orogenic Belt. *Gondwana Research, 43*, 123–148. https://doi.org/10.1016/j.gr.2016.03.013

Liu, Y., Li, W., Ma, Y., Feng, Z., Guan, Q., Li, S., Chen, Z., et al. (2021). An orocline in the eastern Central Asian Orogenic Belt. *Earth Science Reviews, 221*, Article 103808. https://doi.org/10.1016/j.earscirev.2021.103808

Ma, G. (2018). Structure style and evolution features in western district of Chifeng of Chifeng-Kaiyuan Fault (in Chinese with English Abstract). *World of Geology, 37*, 791–803. https://doi.org/10.3969/j.issn.1004-5589.2018.03.011

Ma, H., Chu, R., Sheng, M., & Wei, Z. (2019). Sedimentary structures of the Songliao Basin using high-frequency Ps converted wave from local deep earthquakes (in Chinese with English Abstract). *Journal of Geodesy and Geodynamics, 40*, 214–220. https://doi.org/10.14075/j.jgg.2020.02.019

Mavko, G., Mukerji, T., & Dvorkin, J. (2020). *The rock physics handbook* (3rd ed.). Cambridge University Press. https://doi.org/10.1017/9781108333016

Pan, G., Xiao, Q., Lu, S., Deng, J., Feng, Y., Zhang, K., Zhang, Z., et al. (2009). Subdivision of tectonic units in China (in Chinese with English Abstract). *Geology in China, 36*, 1–28.

Shinjiro, M., Ji' an, S., & Qinglong, Z. (1990). The Nadanhada Terrane in relation to mesozoic tectonics on continental margins of East Asia. *Acta Geologica Sinica – English Edition, 3*, 15–29. https://doi.org/10.1111/j.1755-6724.1990.mp3001003.x

Sjögren, B. (1984). *Shallow refraction seismics*. Springer. https://doi.org/10.1007/978-94-009-5546-2

Tang, Z., Julià, J., Mai, P. M., Mooney, W. D., & Wu, Y. (2022). Shear-wave velocity structure beneath Northeast China from joint inversion of receiver functions and Rayleigh wave phase velocities: Implications for intraplate volcanism. *Journal of Geophysical Research: Solid Earth*. https://doi.org/10.1029/2022JB023956

Tao, K., Niu, F., Ning, J., Chen, Y. J., Grand, S., Kawakatsu, H., Tanaka, S., et al. (2014). Crustal structure beneath NE China imaged by NECESSArray receiver function data. *Earth and Planetary Science Letters, 398*, 48–57. https://doi.org/10.1016/j.epsl.2014.04.043

Wang, C., Sun, Q., & Xie, X. (2022a). Sediment deformation triggered by underlying magma intrusion. *Journal of Asian Earth Sciences, 225*, Article 105045. https://doi.org/10.1016/j.jseaes.2021.105045

Wang, H., Fan, T., & Wu, Y. (2015). The subsurface structure and stratigraphic architecture of rift-related units in the Lishu depression of the Songliao Basin, China. *Journal of Asian Earth Sciences, 99*, 13–29. https://doi.org/10.1016/j.jseaes.2014.11.026

Wang, P. J., Mattern, F., Didenko, N. A., Zhu, D. F., Singer, B., & Sun, X. M. (2016). Tectonics and cycle system of the Cretaceous Songliao Basin: An inverted active continental margin basin. *Earth Science Reviews, 159*, 82–102. https://doi.org/10.1016/j.earscirev.2016.05.004

Wang, R., Li, Z., Bao, F., Xie, J., & Zhao, J. (2019). S-wave velocity structure of sediment in Songliao Basin from short-period ambient noise tomography (in Chinese with English Abstract). *Chinese Journal of Geophysics, 62*, 3385–3399. https://doi.org/10.6038/cjg2019M0144

Wang, X., Wang, R., Shi, W., Tang, D., Xu, L., & Feng, Q. (2022b). Tectonic characteristics and evolution of typical rift basins in eastern China: A case study in the Gudian area, Songliao Basin (in Chinese with English Abstract). *Bulletin of Engineering Geology and the Environment, 41*, 85–95. https://doi.org/10.19509/j.cnki.dzkq.2022.0089

Wei, H.-H., Liu, J.-L., & Meng, Q.-R. (2010). Structural and sedimentary evolution of the southern Songliao Basin, northeast China, and implications for hydrocarbon prospectivity. *AAPG Bulletin, 94*, 533–566. https://doi.org/10.1306/09080909060

Wessel, P., Smith, W. H. F., Scharroo, R., & Luis, J. (2013). Generic mapping tools: Improved version released. *EOS, Transactions of the American Geophysical Union, 94*, 409–410. https://doi.org/10.1002/2013eo450001

Xiao, W., Windley, B. F., Hao, J., & Zhai, M. (2003). Accretion leading to collision and the Permian Solonker suture, Inner Mongolia, China: Termination of the central Asian orogenic belt. *Tectonics, 22*, 1069. https://doi.org/10.1029/2002TC001484

Xu, Z., Xu, Q., Liu, A., Wang, N., Li, G., Peng, C., Yan, L., et al. (2020). The cretaceous stratigraphy, Songliao Basin, Northeast China: Constrains from drillings and geophysics. *Open Geosciences, 12*, 1212–1223. https://doi.org/10.1515/geo-2020-0188

Yang, C., & Niu, F. (2019). Sedimentary structure of the western Bohai Bay basin and other basins in North China revealed by frequency dependent P-wave particle motion. *Geodesy and Geodynamics, 10*, 372–381. https://doi.org/10.1016/j.geog.2018.04.007

Zhang, H., Lei, J., Song, X., & Deng, Y. (2025). Direct surface-wave tomography from ambient noise in the Shanxi Rift Zone and adjacent areas (in Chinese with English Abstract). *CT Theory and Applications, 34*, 175–189. https://doi.org/10.15953/j.ctta.2025.002

Zhang, K., Chen, Q., & Chen, Y. (2020). Crustal structure beneath the southwestern Xing'an-Mongolia Orogenic Belt revealed by receiver function analysis (in Chinese with English Abstract). *Chinese Journal of Geophysics, 63*, 1–21. https://doi.org/10.6038/cjg2020N0048

Zhang, L., & Tian, X. (2024). Pn-wave receiver function. *Journal of Geophysical Research: Solid Earth*. https://doi.org/10.1029/2023JB028318

Zhang, R., Kuang, C., Zhang, X., & Li, Y. (2023). Advances in passive seismic analysis of sediment structure and applications in some typical basins (in Chinese with English Abstract). *Reviews of Geophysics and Planetary Physics, 54*, 12–26. https://doi.org/10.19975/j.dqyxx.2021-063

Zhou, J.-B., & Wilde, S. A. (2013). The crustal accretion history and tectonic evolution of the NE China segment of the Central Asian Orogenic Belt. *Gondwana Research, 23*, 1365–1377. https://doi.org/10.1016/j.gr.2012.05.012

(Received September 20, 2025, revised December 9, 2025, accepted December 11, 2025)